Research Square

Preprints are preliminary reports that have not undergone peer review.
They should not be considered conclusive, used to inform clinical practice,
or referenced by the media as validated information.

# Microstructural and Mechanical Properties of Additive Friction Stir Deposited Aluminum 7050 Alloy

**Krishna Prasad Joshi**

kjoshi1@unm.edu

University of New Mexico - Albuquerque: The University of New Mexico https://orcid.org/0009-0002-3588-6342

**Surya T. Bijjala**

University of New Mexico - Albuquerque: The University of New Mexico

**Anil Lama**

FIU: Florida International University

**Chad Beamer**

Quintus Technologies AB

**Jackson Hisee**

Quintus Technologies AB

**Nick Palya**

Solvus Global LLC

**Rumman Ahsan**

Solvus Global LLC

**Sean Langan**

Solvus Global LLC

**Arvind Agarwal**

Virginia Commonwealth University

**Tyler Dolmetsch**

FIU: Florida International University

**Tanaji Paul**

FIU: Florida International University

**Sohail M.A.K. Mohammed**

UTEP: The University of Texas at El Paso

**Pankaj Kumar**

University of New Mexico - Albuquerque: The University of New Mexico

**Research Article**

**Keywords:** Additive Friction Stir Deposition, Aluminum 7050 alloy, Mechanical properties, Friction-based Solid-State Additive manufacturing, Hot isostatic pressing, Microstructure, Fracture Mechanism

**Posted Date:** October 9th, 2026

**DOI:** https://doi.org/10.21203/rs.3.rs-11167946/v1

**License:** This work is licensed under a Creative Commons Attribution 4.0 International License.
Read Full License

**Microstructural and Mechanical Properties of Additive Friction Stir Deposited Aluminum 7050 Alloy**

Krishna P. Joshi[a], Surya T. Bijjala[a], Anil Lama[b], Chad Beamer[c], Jackson Hisee[c], Nick Palya[d], Rumman Ahsan[d], Sean Langan[d], Arvind Agarwal[b,e], Tyler Dolmetsch[b], Tanaji Paul[b], Sohail M.A.K. Mohammed[b,f,*], Pankaj Kumar[a,*]

[a]Department of Mechanical Engineering, University of New Mexico, Albuquerque, NM 87131
[b]Department of Mechanical and Materials Engineering, Florida International University, Miami, FL 33174
[c]Quintus Technologies, LLC, 8270 Green Meadows Drive North, Lewis Center, OH 43035
[d]Solvus Global LLC, 104 Prescott Street, Worcester, MA 01605
[e]Department of Mechanical and Nuclear Engineering, Virginia Commonwealth University, Richmond, VA 23284
[f]Department of Aerospace and Mechanical Engineering, University of Texas at El Paso, El Paso, TX 79968

*Corresponding author: Pankaj Kumar, Sohail M.A.K. Mohammed
Email: pankaj@unm.edu; smmohammed@utep.edu

**Abstract**

Solid-state Friction Stir Additive Manufacturing offers a melt-free route to produce high-strength aluminum alloys by avoiding the solidification defects that limit conventional fusion-based AM. In this study, AA7050 was deposited by AFSD and subsequently subjected to hot isostatic pressing to eliminate the effects of defects/pores and unbonded regions on tensile behavior. As-deposited AFSD AA7050 retained most of the wrought tensile strength (UTS ≈ 404–468 MPa, versus ≈ 507 MPa for wrought AA7050) and exhibited comparable hardness (~175 ± 5 HV), yet failed with ~ zero uniform elongation compared with ~19% for the wrought AA7050. EBSD revealed a clear layer/interlayer hierarchy comprising coarse, elongated grains in the layer interiors and ultra-fine equiaxed grains concentrated in reheated interlayers. XRD showed an α-Al-dominated matrix in AFSD with the absence of discrete second-phase reflections. Fractography, however, demonstrated that macroscopic embrittlement was primarily governed by large pores and lack-of-bond defects at interlayer boundaries. Cracks initiated and propagated along these defects, while regions between them exhibited shallow dimples, characteristic of ductile micro-void coalescence in AA7050. Hot Isostatic Pressing (HIP) removed the large defects and homogenized the microstructure, but also severely coarsened the η′/η precipitates. Consequently, HIPed AFSD AA7050 exhibited reduced strength (UTS ≈ 316–324 MPa) but showed improved ductility (~18–19% elongation) comparable to the wrought AA7050. The results quantitatively demonstrate a strong trade-off between defect elimination and precipitation, and highlight that AFSD process design for AA7050 must simultaneously control porosity, interlayer bonding, and precipitate stability to achieve wrought-like strength–ductility combinations without over-reliance on aggressive HIP treatments.

**Keywords:** Additive Friction Stir Deposition; Aluminum 7050 alloy; Mechanical properties; Friction-based Solid-State Additive manufacturing; Hot isostatic pressing; Microstructure; Fracture Mechanism

# 1 Introduction

High-strength, precipitation-hardened aluminum alloys in the 7xxx series remain core structural materials for airframes because they combine high specific strength with fatigue and damage-tolerance performance at relatively low cost. Aluminum 7050, an Al–Zn (<6%)–Mg (<3%)–Cu (<3%) alloy, is widely used in primary load-bearing components due to its balanced strength, higher specific strength, fracture toughness, and stress-corrosion cracking resistance [1–3]. Conventional forming methods for AA7050, such as casting, forging, extrusion, and rolling, produce components with excellent mechanical properties but are restricted in geometric complexity and material utilization. In addition, the fabrication and repair of AA7050 components using conventional fusion-based processing routes remain challenging due to hot cracking, segregation, porosity formation, and uncontrolled precipitation during solidification [4,5]. These limitations have motivated increasing interest in solid-state additive manufacturing (AM) approaches that can mitigate melting-related defects while enabling near-net-shape fabrication [5–8]. Fusion-based AM, such as laser powder bed fusion and directed energy deposition, has limited success in manufacturing AA7xxx-series alloys. During fusion AM, rapid solidification and repeated thermal cycling lead to solute segregation, porosity, liquation, and solidification cracking, which deteriorate both strength and ductility [6,7,9]. Furthermore, the volatility of Zn and Mg in high-temperature melt pools alters alloy chemistry and reduces hardening potential [8,10–12]. These metallurgical limits create a persistent gap between the geometric flexibility promised by metal AM and what can be reliably achieved for aerospace-grade 7050 components using beam-based routes [1,13]. These limitations have driven research toward solid-state AM approaches, which eliminate melting and rely on severe plastic deformation and frictional heating to consolidate layers.

Additive Friction Stir Deposition (AFSD) has recently emerged as a promising solid-state additive manufacturing technique that leverages severe plastic deformation and frictional heating to build fully dense metallic components layer-by-layer without melting [1,3–5,14–18]. In AFSD, feedstock material undergoes intense shear deformation under elevated temperatures, promoting dynamic recrystallization, extensive grain refinement, and strong texture evolution [8,16]. Unlike laser-based AM processes, AFSD avoids solidification-driven microstructural heterogeneity, offering the potential for superior mechanical integrity and compositional uniformity in high-strength aluminum alloys. Despite these advantages, the fundamental relationships between AFSD processing, microstructural evolution, and phase stability in precipitation-strengthened 7xxx alloys remain incompletely understood [5,19].

The additional benefits of AFSD include high deposition rates, low porosity, repair capability for valuable structures, and the capacity to consolidate dissimilar or recycled feedstocks while preserving near-wrought properties [8]. At the same time, AFSD introduces its own microstructural signature, such as layer-wise thermal cycling, gradient precipitation states through the build height, and anisotropy tied to material flow and tool kinematics [18,20]. These features can be leveraged through parameter optimization and heat treatment, but they also require careful control to mitigate effects such as abnormal grain growth or interface-localized corrosion in multilayer builds [4,14,21–23].

Several studies have documented the wrought-like microstructures and properties of as-deposited and heat-treated Aluminum 7050 produced by friction-based solid-state manufacturing and AFSD processes [4,5,22,23]. Hahn et al.[21] demonstrated that AFSD AA7050 followed by T74 aging achieved YS ≈ 430 MPa, UTS ≈ 491 MPa, and elongation ≈ 11.2%, i.e., “forging-like” properties without composition modification, highlighting the viability of standard feedstock and conventional aging practice. Similarly, Mason et al.[17] quantified microstructural refinement and spatially varying tensile response across regions with different thermomechanical histories in an AA7050 AFSD build. Rojas et al. [16] showed improved bonding and tensile performance using AFSD. Recent work has shown that lubricant-free AFSD AA7050

can achieve “tensile build-direction heat-treated T74 forging properties,” emphasizing the role of aging time in converging on the target strength–ductility window for aerospace-relevant directions[21].

Severe plastic deformation during AFSD is expected to profoundly alter features such as grain boundary character, dislocation density, and precipitation distribution by promoting continuous dynamic recrystallization, solute redistribution, and the suppression of equilibrium precipitate formation [5,8,24]. However, the extent to which AFSD modifies these relative to thermally equilibrated conditions such as HIP has not been systematically investigated. In particular, region-specific variations in grain size and grain boundary character across AFSD deposits, and their connection to deformation-driven phase evolution, remain largely unexplored [5,8,13,14,20].

Existing literature and work on friction-based solid-state AM largely emphasize avoiding hot cracking and gross porosity relative to fusion AM, and treat the main challenges as control of thermal history, recrystallization, texture, and aging response rather than manufacturing defects such as unbonded regions and interlayer/interfacial pores within as-deposited materials [5,8,14]. For Al–Zn–Mg–Cu systems, Mason et al. [17] selected AFSD process windows to produce “fully dense” deposits and attributed strength gradients to local over-aging and precipitate coarsening. In their study, they reported that the fracture was controlled by particle-nucleated void growth rather than large lack-of-bond pores. Post-processing treatment/repair-oriented AFSD studies on AA7050 and related alloys 7A56,7055 have shown that wrought-like yield and ultimate strengths can be recovered after standard T6/T7 tempers [23,25]. The associated scatter and loss of ductility were linked qualitatively to microstructural inhomogeneity and interfacial voids/pores, without systematic quantification or treatment of these defects as design variables [1]. The present work addresses this gap by explicitly quantifying unbonded regions and interfacial pores in as-deposited AFSD AA7050, linking pore morphology and area fraction to fracture mechanisms and fracture regime. Besides that, this work demonstrates that HIPing can eliminate these extreme defects and recover ductile behavior comparable to wrought AA7050.

In this work, the microstructural and phase evolution of AA7050 processed by AFSD is comprehensively investigated and correlated with its tensile behavior. The tensile strength of as-deposited and post-hot isostatic pressing (HIP) AFSD AA7050 is measured, compared, and analyzed in relation to the defects observed via fractography. Quantitative microstructural characterization is performed to correlate microstructural features with the observed mechanical properties across distinct processing conditions. By integrating these microstructural and phase analyses, this study elucidates the unique deformation-dominated microstructural state produced by AFSD and its implications for tailoring high-performance AA7050 components.

## 2 Experimental Method

### 2.1 Material Deposition

AFSD of AA7050 was carried out at Solvus Global using a Bond Technologies GL7 friction stir deposition instrument operating in force-controlled mode. In this configuration, the deposition system continuously modulates the consumable feedstock feed rate to maintain a constant axial load during processing. The tool employed for this study was a textured shoulder head incorporating teardrop-shaped protrusions, a design selected to enhance frictional heat generation, to intensify shear deformation, and promote uniform plastic flow across the deposition interface. Prior works have demonstrated that such textured features improve material stirring efficiency and reduce the likelihood of interlayer defects in high-strength aluminum alloys deposited through

solid-state additive routes [2,5,19,21]. Deposition was performed under a constant axial force limit of 14 kN, with the feed rate automatically adjusted in real time to maintain this load. Although the feed rate varied during the processing, the nominal value stabilized near 35 mm/min. A two-stage rotational speed profile was used, i.e., the tool rotated at 450 rpm during the pre-heat stage to raise the substrate-tool interface temperature, and after that the rotation was reduced to 250 rpm for uniform material deposition on the pure aluminum substrate. The tool traverse speed was maintained at 150 mm/min throughout all layers. The schematic diagram of the AFSD process used in the experiment is shown in Fig. 1(a). Using these conditions, a fully dense AFSD-manufactured AA7050 block was produced with final dimensions of 100 mm × 23 mm × 19 mm on a 10 mm substrate. Fig. 2(a) shows the fabricated AA7050 block. The specimen was made by using AA7050 feedstock by depositing 96 layers in total. The density was evaluated by the Archimedes method, yielding 99.85% density, which indicates near-full consolidation. The wrought AA7050 material was used as a reference to compare its mechanical properties with those of the as-deposited and post-processed AFSD AA7050. The commercial wrought AA7050 was procured from McMaster-Carr in the AA7050-T7451 temper condition. This temper consists of solution heat treatment up to 537 °C followed by rapid cooling and stress relief by controlled stretching, and artificial over-aging at approximately 204 °C.

### 2.2 Post-Deposition Treatment

A half portion (50mm x 23mm x 19mm) of the as-deposited AA7050 material was also subjected to HIPing to assess the extent to which post-deposition densification and homogenization could further improve mechanical properties. HIP processing was carried out at Quintus Technologies, LLC. The HIP cycle involved ultra-high-purity (99.995%) argon gas pressurization to 100 MPa at 470°C with a 4-hour hold, followed by furnace cooling. The selected temperature remains slightly below the typical solution-treatment temperature range for AA7050, thereby facilitating full densification and microstructural homogenization of the sample. Such HIP parameters have also been adopted in prior studies of friction-stir-based AM and are known to reduce microstructural heterogeneity introduced by layer-wise thermal cycling [10,11,22,26].

The as-deposited and post-HIP material sections were subsequently machined and prepared for microstructural and mechanical characterization using standard metallographic grinding and polishing procedures. The polished surface was examined using a scanning electron microscope (SEM, JSM F100, JEOL Ltd., Japan) equipped with a high-resolution electron backscatter diffraction (EBSD) detector (Symmetry S2, Oxford Instruments, UK). EBSD scans were conducted at an accelerating voltage of 20 kV with a step size of 0.1 μm. The data collected were analyzed using Aztec Crystal, an EBSD post-processing software from Oxford Instruments, UK.

### 2.3 Mechanical Testing

The miniature tensile specimens were extracted from the block in the build direction using wire electrical discharge machining (EDM) to avoid microstructural alteration in the gauge region, as shown in Fig. 2(a). The tensile geometry of the extracted miniature tensile specimen is shown in Fig. 1(b) [27]. All specimens were lightly surface-finished along the gauge length to remove EDM recast layers without modifying critical dimensions. Mechanical testing was conducted at room temperature at a strain rate of $1 \times 10^{-3}$ per gauge length per second using miniature specimens.

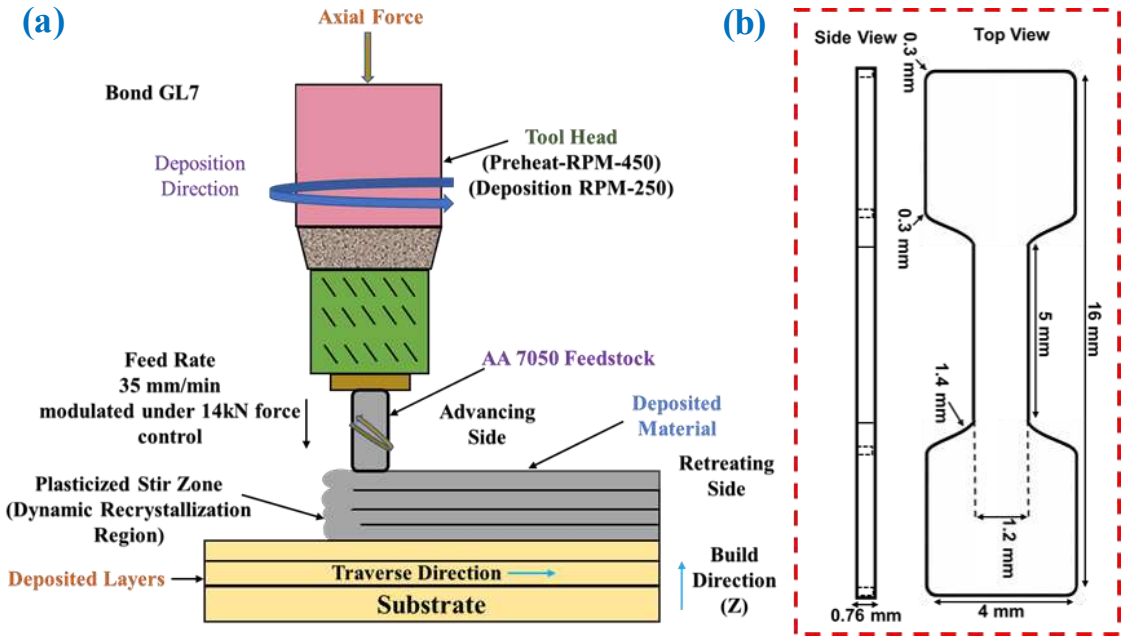



**Fig. 1.** (a) Schematic Diagram of AFSD Process and (b) geometry of miniature tensile specimen [26].

## 3 Results

### 3.1 Microstructure

ASFD imposes severe plastic deformation and complex thermal cycles, refining grains by dynamic recrystallization (DRX) and generating high dislocation densities that could strongly influence mechanical behavior. To quantify these effects in AFSD-ed AA7050 deposits, electron backscattered diffraction (EBSD) was performed, capturing multiple deposited layers across the deposit thickness at the location marked in Fig. 2(a), providing inverse pole figure (IPF) maps and Kernel Average Misorientation (KAM)

maps. EBSD reveals a dual-heterogeneous microstructure comprising alternating fine-grained (FG) and

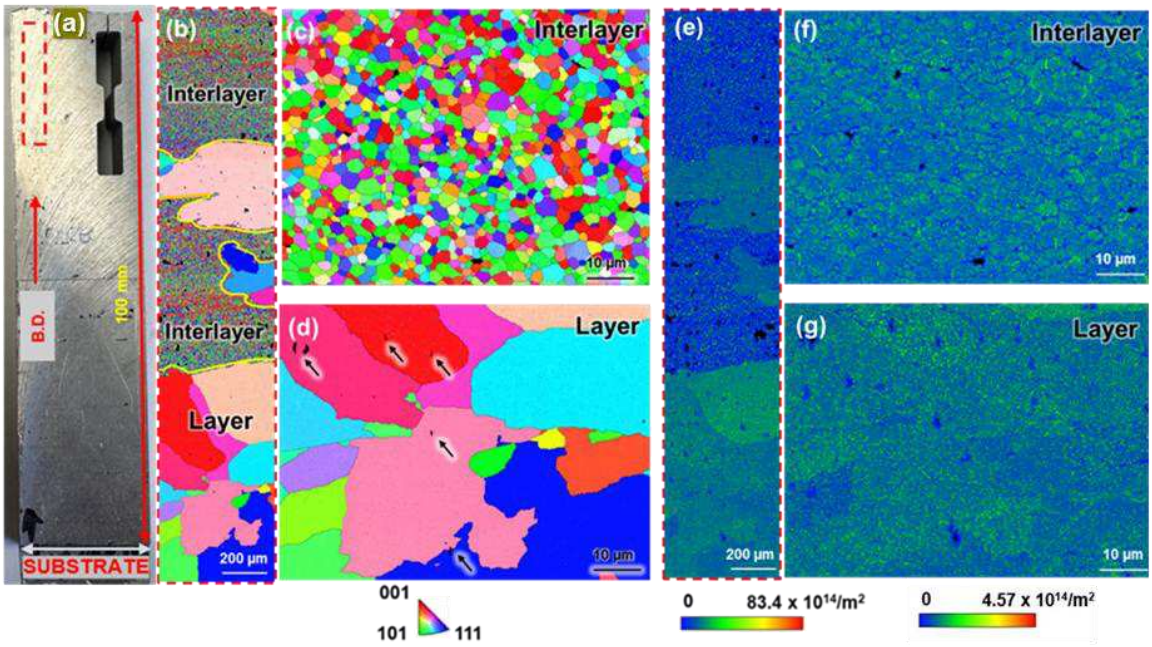



**Fig. 2.** (a) Macrograph of the AFSD as-deposited AA7050 showing the build direction (B.D.) and the EBSD scan location (by red dotted rectangle) and region from tensile samples were extracted (tensile shape hollow cavity). (b) Through-thickness inverse pole figure (IPF) map with grain boundaries: high-angle grain boundaries (HAGBs, >15°) showing alternating fine (interlayer)- and coarse-grained (Layer) regions. (c, d) Magnified IPF maps of the fine (interlayer)- and coarse-(Layer) grained regions, respectively. (e) Kernel Average Misorientation (KAM) map, with (f, g) magnified views of the fine (interlayer)- and coarse (interlayer)-grained regions.

coarse-grained (CG) regions across the build, confirming a bimodal grain size distribution. This bimodality is clearly visible in the IPF map in Fig. 2(b), where FG regions exhibit equiaxed grains (Fig. 2c) with an average grain size of 2.6 ± 0.9 µm, while CG regions reach 501 ± 161 µm. The bimodality is attributed to the heterogeneity in the interfaces and layers. The FGs correspond to the interlayer, whereas the CGs correspond to the layers. The broad color distribution in the IPF map indicates a nearly random crystallographic orientation with no dominant texture along the build direction, suggesting that grain formation is primarily governed by local strain and thermal conditions. The grain boundary character differs significantly between regions (Table 1, Fig. 2(c, d)): FG regions contain 77.8% high-angle grain boundaries (HAGBs, >15°) and 22.2% low-angle grain boundaries (LAGBs, 2–15°), whereas CG regions contain 44.2% HAGBs and 55.8% LAGBs. The high fraction of HAGBs in FG regions indicates extensive continuous DRX, where sub-grain boundaries accumulate dislocations and progressively rotate to form HAGBs. The LAGB-rich CG regions reflect dominant dynamic recovery and incomplete recrystallization. This duality in microstructural evolution arises from the spatially and temporally heterogeneous thermomechanical conditions inherent to AFSD: newly deposited layers experience intense severe plastic deformation, forming ultrafine grains, while previously deposited material is partially reheated. These observations are in contrast with the DRX behavior reported for AA7050 and AA7075 processed by AFSD and other friction-based additive routes [5,8,14,28]. Mason et al. [17] showed that as-deposited AFSD AA7050 develops a recrystallized, equiaxed grain structure throughout the deposit, with grain diameters

typically in the range of a few micrometers and a relatively uniform grain reference orientation spread, reflecting a homogeneous thermomechanical history within the bulk stir zone. Girault et al.[20] similarly reported equiaxed grains of a few to ~20 μm in an AFSD AA7075 wall, with modest vertical gradients in grain size arising from variations in the local Zener–Hollomon parameter but without strongly discrete interlayer bands [5,20]. In the present AFSD build, the interlayer refinement is more pronounced, and the microstructural contrast between layers and interlayers is sharper than in those reported AFSD studies [23,29]. This difference is attributed to the distinct process kinematics in plate-based AFSD compared with center-fed AFSD. In AFSD, each new layer experiences intense shear at its upper surface during welding to the underlying layer, while the interior of the previously formed layer is primarily subjected to thermal cycling. As a result, interlayers record the highest strain and strain rate and undergo extensive continuous DRX, while the layer interiors experience only recovery and limited grain growth. Additionally, the upper portion of existing layers acts as a heat sink, promoting grain growth and the formation of CG regions, whereas the lower portions retain ultrafine grains. Repeated layer-by-layer thermal cycling thus amplifies these differences, producing the observed alternating FG–CG banded structure throughout the deposit thickness.

Table 1. Average grain size, distribution of LAGBs, HAGSs, and GNDs in as-deposited and HIPed AA7050 AFSD deposits.

| | Average grain size (μm) | LAGB (%) | HAGB (%) | GNDs (x $10^{14}/m^2$) |
|---|---|---|---|---|
| As-Deposited (Fine-grain region) | 2.6 ± 0.9 | 22.2 | 77.8 | 83.35 |
| As-Deposited (Coarse-grain region) | 501 ± 161 | 55.8 | 44.2 | 4.51 |
| HIPed | 71 ± 180 | 65.1 | 34.9 | 2.28 |

The KAM maps in Fig. 2(e) provide a quantitative measure of the distinct deformation histories within the deposit. FG bands exhibit a very high average GND density of $83.35 \times 10^{14}$ $m^{-2}$, whereas CG bands show only $4.51 \times 10^{14}$ $m^{-2}$, yielding a ratio of ~18.5:1. This contrast indicates that FG regions experience intense plastic deformation, resulting in strong orientation gradients and high stored elastic energy due to strain incompatibility both within and between grains. These accumulated dislocations act as effective pinning centers for grain boundaries, generating back stresses that hinder boundary migration and suppress grain growth. Consequently, ultrafine grains are preserved in regions subjected to continuous DRX. In contrast, the lower GND density observed in CG regions suggests that dynamic recovery has been more effective. Dislocation annihilation and rearrangement reduce orientation gradients and stored energy, lowering the driving force for further recrystallization and removing obstacles to grain boundary motion. Combined with a higher fraction of LAGBs, this facilitates boundary migration under the thermal exposure of AFSD, enabling rapid grain coarsening. Therefore, the coexistence of low GND density and incomplete conversion of LAGBs to HAGBs is consistent with partially recovered sub-grain structures that grow during subsequent heating.

These features suggest a high density of low-angle boundaries and residual dislocations retained after DRX, which is expected for ultra-fine grains formed under high Zener–Hollomon conditions [5,30]. In comparison, the coarser grains within the layer bands show a more uniform KAM distribution, suggesting

lower intragranular lattice distortion and partial recovery. A similar interplay between DRX-refined regions and recovered coarse grains was reported by Girault et al [20] for AFSD AA7075. Additionally, EBSD micrographs for the as-deposited condition also show the presence of fine pores and voids (black spots in Fig. 2 (f, g) in the microstructure, which are identified as common manufacturing defects in AFSD AA7050.

Microstructural evolution during HIP was examined by EBSD at three different locations within the AFSD AA7050 HIPed sample. Fig. 3 presents the representative inverse pole figure (IPF), and kernel average misorientation (KAM) map. The quantitative grain-size, grain-boundary, and GND-density data are also summarized in Table 1. The HIPed condition exhibits an irregular and predominantly non-equiaxed grain structure with no clearly distinguishable layer or interlayer bands. This differs significantly from the as-deposited material, in which fine grains were concentrated within the interlayers, and coarse grains were present in the layer interiors.

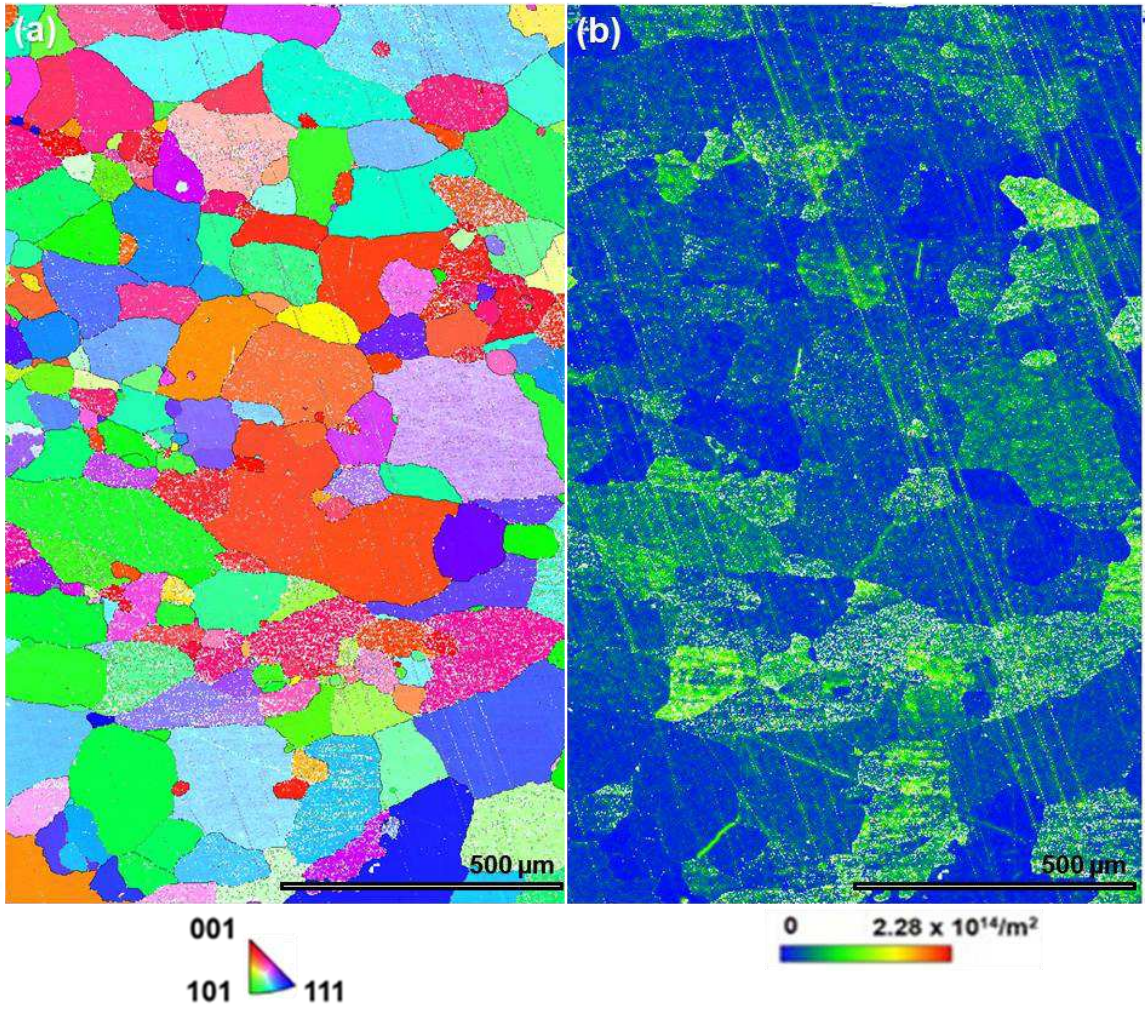



Fig. 3. EBSD of the AFSD AA7050 HIPed showing the representative scan area of three different regions; (a) Magnified IPF maps of the region with (b) corresponding KAM maps.

The average grain size after HIP was 71 ± 180 μm, compared with 2.6 ± 0.9 μm in the fine-grained interlayers and 501 ± 161 μm in the coarse-grained layer regions of the as-deposited condition. The large standard deviation in the HIPed sample shows a broad grain-size distribution rather than a uniformly recrystallized structure. HIP therefore reduced the sharp bimodal contrast of the as-deposited microstructure by promoting substantial growth of the ultrafine interlayer grains and modifying the morphology of the coarse layer grains. The disappearance of discrete layer and interlayer bands indicates extensive grain-boundary migration and redistribution of the deformation-generated microstructure during the high-temperature exposure.

The grain-boundary distribution in AFSD AA7050 also changed substantially after HIP. The HIPed sample contained approximately 65.1% low-angle grain boundaries (LAGBs) and 34.9% high-angle grain boundaries (HAGBs). In comparison, the fine-grained and coarse-grained regions of the as-deposited material contained 22.2 and 55.8% LAGBs, respectively. The high LAGB fraction after HIP shows that a considerable proportion of the deformation-induced dislocations rearranged into lower-energy subgrain boundaries [22,31,32]. The retained LAGB network, together with the predominantly non-equiaxed grain morphology, suggests that recovery was more extensive than complete recrystallization. Nevertheless, the presence of HAGBs and the elimination of the ultrafine interlayer bands indicate that grain-boundary migration and partial recrystallization also contributed to the final microstructure [5,10,26,30].

The KAM map (Fig. 3 (c)) further demonstrates the reduction in stored deformation following HIP. The average GND density calculated from the KAM map decreased to $2.28 \times 10^{14}$ $m^{-2}$ in the HIP sample, compared with $83.35 \times 10^{14}$ $m^{-2}$ in the fine-grained interlayers and $4.51 \times 10^{14}$ $m^{-2}$ in the coarse-grained regions of the as-deposited sample. The significant decrease relative to the fine-grained interlayers confirms substantial recovery, i.e., annihilation and rearrangement of deformation-induced dislocations during the HIP thermal cycle. The KAM map is dominated by low-density blue regions, while localized green-to-yellow regions near grain and subgrain boundaries suggest residual dislocation accumulation and lattice distortion. Similar reductions in dislocation density and microstructural anisotropy after HIP have been reported in AM metallic systems, where exposure at elevated temperature promotes recovery and recrystallization while isostatic pressure assists defect closure [26,33].

While the direct EBSD studies of HIPed AFSD AA7050 remain limited, Gussev et al. [26] reported that HIP modified bonded interfaces and promoted recrystallization in ultrasonic AM aluminum. Although ultrasonic additive manufacturing and AFSD involve different deformation conditions, both are solid-state, layer-based processes; therefore, the disappearance of the layer/interlayer distinction in the present material is consistent with the homogenization of interface-dominated microstructures reported after HIP. Recovery, recrystallization, grain growth, and reduction of microstructural anisotropy are also widely identified as consequences of HIP thermal exposure in additively manufactured metals [33].

The EBSD results demonstrate that HIP transformed the sharply bimodal as-deposited grain architecture into a continuous but still heterogeneous grain-size distribution. The ultrafine interlayer grains underwent substantial growth, the original layer/interlayer morphology disappeared, and the GND density decreased drastically. The retained LAGB network and low GND density indicate extensive recovery and subgrain formation, while the remaining HAGBs and modified grain morphology indicate concurrent boundary migration and partial recrystallization.

These microstructural changes, particularly grain growth, dislocation annihilation, and the reduction in stored deformation, have been widely associated with diminished strengthening contributions in heat-treated additively manufactured aluminum alloys [10,22,25,29,33,34].

Fig. 4. shows the SEM microstructure of the HIPed AFSD AA7050. The low magnification microstructure (Fig. 4 (a)) shows the presence of the precipitate phase in the grain interior and at the grain boundaries. At higher magnification, particles are dispersed within the grains and along the grain boundaries, while fine

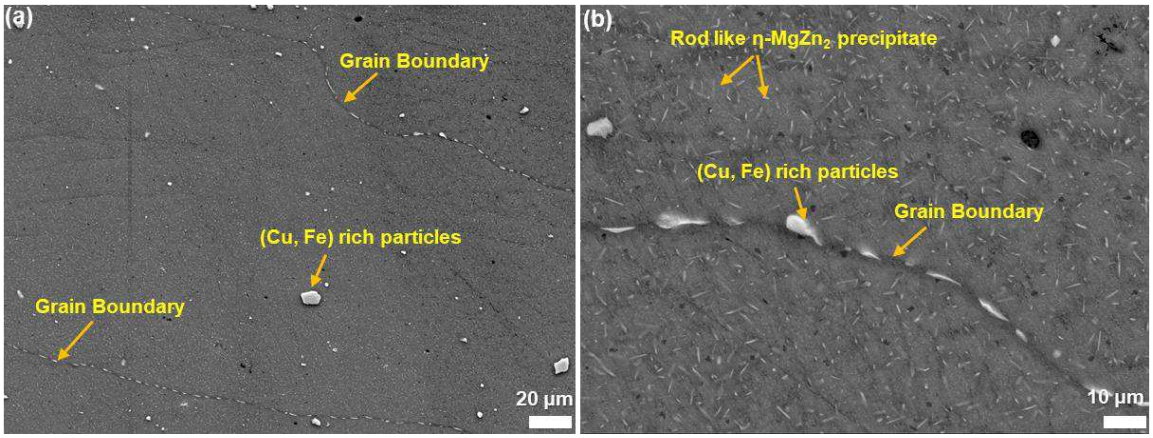



**Fig 4** SEM micrographs of the HIPed AA7050 (a) showing the grain boundary and (Cu, Fe) rich particles along with the (b) presence of fine rod-like η-$MgZn_2$ precipitates at higher magnification

elongated rod-like η-$MgZn_2$ precipitates are distributed uniformly throughout the matrix along with the particle shape precipitates as shown in Fig 4 (b).

The EDS maps obtained from one of the coarse particles in Fig 4 (a) are shown in Fig 5. The particle exhibits strong enrichment in Fe and Cu. No clear enrichment of Mg or Zn is observed within the particle. The particle is therefore mostly an Fe-Cu-rich constituent intermetallic, plausibly an $Al_7Cu_2Fe$-type phase [10,11,35]. Coarse $Al_7Cu_2Fe$ particles are widely reported as principal constituent intermetallics in wrought AA7050 and can occur at the micrometer scale [36]. Mason et al. similarly identified $Al_7Cu_2Fe$ as a dominant coarse constituent-particle population in AFSD-processed AA7050 [17].

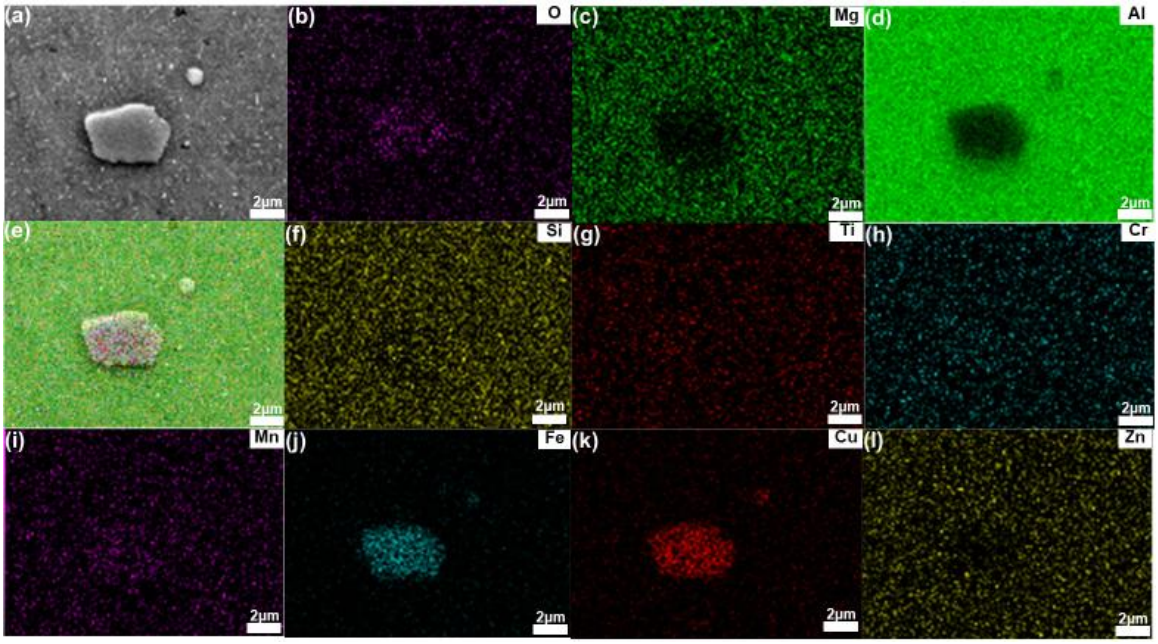



**Fig 5.** EDS map of the HIPed sample on the highly magnified (a) particle region from Fig.4 (a); showing the elemental distribution of (b) oxygen (c) Magnesium (d) Aluminum (e) combined EDS maps of all elements (f) Silicon (g) Titanium (h) Chromium (i) Manganese (j) Iron (k) Copper (l) Zinc in the microstructure.

The persistence of the Fe-Cu-rich particles after HIP is expected because Fe-bearing constituent phases exhibit limited solubility in the α-Al matrix during conventional thermal treatment [10]. Studies on high-strength Al-Zn-Mg-Cu alloys have shown that soluble Zn-Mg-Cu-rich phases decrease during elevated-temperature treatment, whereas residual coarse particles are predominantly Fe-rich intermetallics [25]. Thus, HIP alters the surrounding grain structure and precipitate population by partially dissolving and coarsening Al-Cu-Fe particles [10,25,29]. the EDS elemental maps indicated an apparent absence of Al within the particle boundaries. This phenomenon is attributed to an instrumentation artifact involving localized peak auto-scaling and detector signal saturation; the exceptionally high X-ray count rates generated by the dense accumulation of heavy Fe and Cu atoms mathematically suppressed the lower-energy matrix Al signal during automated spectral mapping.[37,38].

Fig. 6 shows the XRD patterns of the as-deposited and HIPed AFSD AA7050 samples. Both conditions are dominated by the α-Al phase. No secondary-phase reflections were observed in the as-deposited condition apart from the α-Al. The relative intensities of the α-Al reflections changed significantly after HIP. The HIPed pattern was dominated mainly by the (111) and (200) reflections, whereas the (220), (311), and (222) reflections were strongly suppressed. Two reflections of the η-$MgZn_2$ phase appeared at approximately 41–$42^0$ in the HIPed pattern. These reflections show that the HIP thermal cycle promoted precipitation, transformation and coarsening of the Mg–Zn-rich phase [34,35,39,40]. Heating studies on Al–Zn–Mg–Cu alloys have similarly shown that the equilibrium η-Mg (Zn, Cu, AL)$_2$ phase can precipitate during exposure at elevated-temperature [22]. The presence of $MgZn_2$-related reflections after HIP indicates an evolution toward a more detectable equilibrium precipitation state rather than an increase in the density of fine strengthening precipitates [3,16,22].

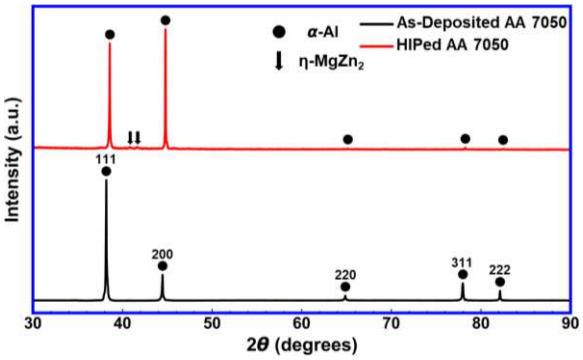



**Fig. 6.** XRD Pattern of As-Deposited AFSD AA7050

XRD analysis of the HIPed AFSD AA7050 alloy identified the presence of the hexagonal η-$MgZn_2$ phase (C14 Laves structure). SEM observations revealed two distinct morphology precipitates within the microstructure: coarse circular particles and elongated, fine rod-like features located primarily within the grain interiors. Because the bulk XRD spectra exclusively indexed to the hexagonal η-$MgZn_2$ framework and completely lacked the characteristic reflections of the orthorhombic S-phase ($Al_2CuMg$), these fine intra-granular rods are identified as coarsened η-$MgZn_2$ precipitates generated during the HIP thermal cycle [39,41,42].

### 3.2 Mechanical properties

#### 3.2.1 Hardness of AFSD AA7050

The Vickers hardness of all three conditions were quantified using 20 indents in each sample. The hardness data are comparatively insensitive to these changes in condition of AA7050: wrought AA7050, AFSD (as-deposited), and AFSD (HIPed) show 176 ± 20 HV, 175 ± 5 HV, and 170 ± 7 HV, respectively. The small spread of standard deviation (≤6 HV) suggests that the local indentation response of the matrix remains broadly similar across all conditions, even though the tensile ductility of as deposited AFSD sample varies drastically compared to the wrought and HIPed AFSD sample. This is plausible because hardness integrates multiple short-range strengthening contributions within the indentation volume (solid solution, dislocation density, and any remaining fine precipitates), whereas tensile elongation is strongly degraded by rare large defects. The slight decrease in hardness after HIP is could be attributed to dissolution or coarsening of η/η′ precipitates [31,23]. The Vickers's hardness test for all the samples is summarized in the Table 2.

Table 2. Vickers's hardness values of Wrought AA7050, AFSD AA7050 (as-deposited) and AFSD AA7050 (HIPed) at room temperature.

| Condition | Hardness (HV) |
|---|---|
| Wrought AA7050 | 176 ± 20 |
| AFSD AA7050 (as-deposited) | 175 ± 5 |
| AFSD AA7050 (HIPed) | 170 ± 7 |

The bulk tensile properties can further manifest and provide overall variation in the mechanical properties with respect to the processing.

### 3.2.2 Tensile properties of AFSD AA7050

The tensile responses of the as-deposited and HIP AFSD AA7050 were assessed and compared with that of the wrought AA7050 reference. The tensile stress strain curve of as-deposited AFSD AA7050, wrought AA7050 and HIPed AA7050 is shown in Fig. 7. The wrought AA7050 exhibited the expected behavior for a peak-aged 7xxx alloy (Fig. 7). After linear elastic loading, the stress-strain curve shows a substantial work-hardening regime and reaches an ultimate tensile strength (UTS) of ~505 ± 1.4 MPa with a total elongation of ~19% as shown in Fig. 7. Fracture occurs after noticeable necking, indicating a stable ductile failure mode. Although the elastic regime is linear and overlaps with the wrought, the as-deposited AFSD specimens show a noticeably different tensile behavior.

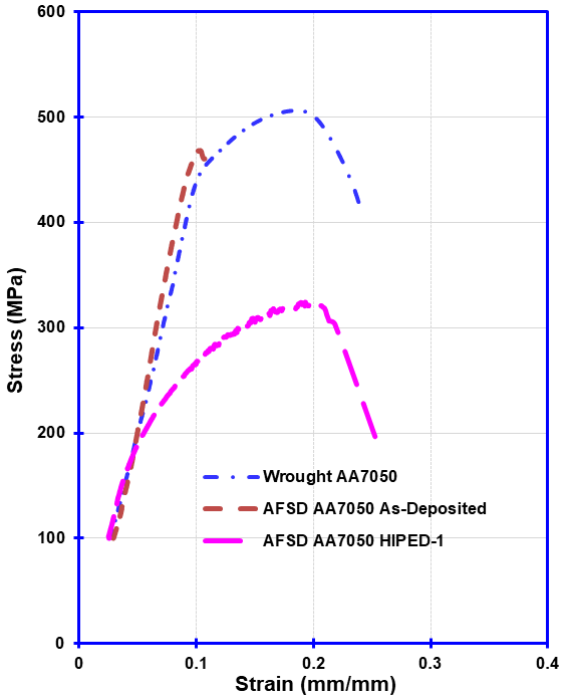



**Fig. 7.** Tensile Stress Strain Curve of As-Deposited AFSD AA7050, Wrought AA7050 and HIPed AA7050.

The measured average UTS for the as-deposited AFSD specimens is 428 ± 35 MPa. However, the as-deposited AFSD samples fractured without exhibiting any yielding or necking. Thus, the overall response can be described as good strength with relatively poor ductility. It must be noted that the average measured UTS value for the three as-deposited AFSD specimens is 428 MPa with a standard deviation of 35 MPa, as shown in Table 3. The variation in their strength, although under identical processing conditions, will be discussed later. This combination of moderately high strength and no ductility is in contrast to what has been reported for as-deposited AFSD AA7050 in the literatures [5,21,23,28]. Mason et al. [17] observed that as-deposited AFSD AA7050 exhibits significantly reduced yield strength compared with wrought T7651 material, but retains appreciable ductility due to a relatively homogeneous recrystallized grain structure and a partially dissolved precipitate state. In their study, the best-performing as- deposited orientation remained roughly 50 MPa below the wrought yield strength, with ductility varying strongly with position in the build yet remaining clearly non-zero. Similarly, AFSD AA7075 alloy in other studies showed reduced UTS and yield strength relative to wrought AA7050, but still exhibited significant elongation in the as-deposited condition [23,28]. In the present AFSD AA7050 system, the loss in strength in as-deposited relative to wrought is less severe, but the complete loss in ductility is much more extreme. Thus, to restore ductility and improve microstructural homogeneity in the AFSD AA7050, part of the as-deposited AA7050 was subjected to HIPing.

Tensile tests performed on the HIPed material reveal a significant shift in the balance between strength and ductility. After HIP, the average UTS of the AFSD specimens decreases to 320 ± 6 MPa, corresponding to approximately 63% of the wrought AA7050 strength. Relative to the as- deposited AFSD state, this

represents a reduction of roughly 20–30% in UTS. Despite this loss in strength, the HIPed material exhibited a significant improvement in ductility of ~18.4%, comparable to that of wrought AA7050. The tensile test results are summarized in Table 3. The post-HIP stress–strain curve in Fig. 7 shows an extended plastic region with clear work hardening before fracture, i.e., a fully ductile failure mode has been restored. The response of the HIPed AFSD material is broadly in line with observations for AFSD AA7050 and other 7xxx alloys subjected to post-deposition thermal treatments [10,29,33]. Mason et al. [17] showed that solution treatment and aging of AFSD AA7050 substantially alter the precipitate fraction, leading to increased strength compared with the as- deposited condition but also creating the risk of over-aging and strength loss if the thermal exposure is excessive. Hahn et al. [21] demonstrated that a carefully controlled T74 treatment applied to AFSD AA7050 can yield "forging-like" tensile properties (UTS ≈ 490 MPa, elongation >11%) when abnormal grain growth is suppressed. In contrast, the HIP treatment adopted here shifts the AFSD material towards a lower-strength but high-ductility state; strength is compromised, yet wrought-level elongation is recovered.

Table 3. Room temperature tensile properties of Wrought AA7050, AFSD AA7050 (as-deposited) and AFSD AA7050 (HIPed).

| Processing | Yield Strength (MPa) | Ultimate Tensile Strength (MPa) | Ductility (%) |
|---|---|---|---|
| Wrought AA7050 | 445 ± 6 | 505 ± 1.4 | 19.15 ± 0.21 |
| As-deposited AFSD AA7050 | - | 428 ± 35 | 0 |
| HIPed AA7050 | 202 ± 7 | 320 ± 6 | 18.4 ± 0.57 |

## 4 Discussion

### 4.1 Tensile behavior of wrought and AFSD AA7050

The fracture behavior of AA7050 in the wrought, as- deposited AFSD, and HIPed AFSD conditions was examined by correlating tensile response with SEM fractography, enabling a direct comparison of how processing-induced defects and microstructural evolution control the transition from ductile to defect-dominated fracture. The wrought AA7050 provides the baseline to study the fracture behavior of AFSD in as-deposited and HIPed conditions, as it exhibits the expected peak-aged 7xxx response, with an ultimate tensile strength of ~507 MPa and total elongation of ~19%. Fig. 8(a) shows a panoramic view of the entire fracture surface, which is macroscopically rough and tortuous, with no evidence of large internal interfacial pores, lack-of-bond defects, or extended planar facets. High-magnification examination (Fig. 8(b)) reveals a uniform carpet of fine, equiaxed dimples. This shows typical ductile failure: the voids grow, impinge on neighboring voids, and coalesce to form the final rupture surface via classic ductile micro-void coalescence [43–45]. Similar dimpled morphologies have been reported for AA7050-T7451 under monotonic loading, [46,47]. Quantitative fractography of 7xxx series alloys shows that a high fraction of such dimples correlates with high ductility and fracture toughness, whereas quasi-cleavage facets or flat regions accompany reduced plasticity [46]. The predominance of fine dimples and the absence of large defects in the present wrought material are therefore in agreement with its high elongation and stable necking prior to failure.

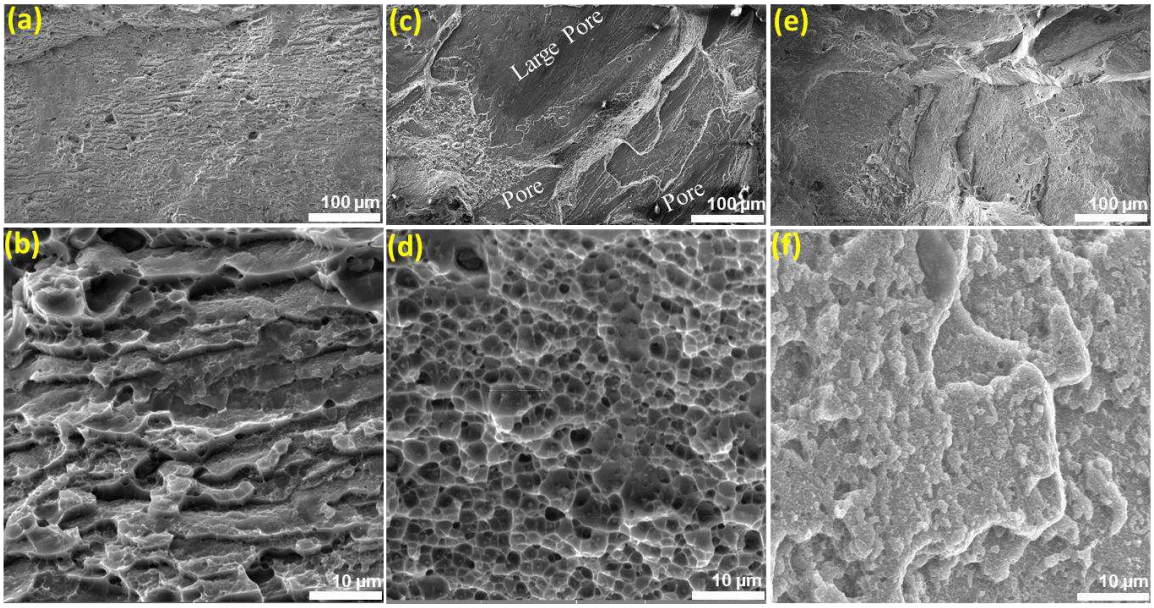



**Fig. 8.** SEM fractography of (a), (b) Wrought AA7050; (c), (d) As-deposited AFSD AA7050; and (e), (f) HIPed AA7050.

In contrast, the as-deposited AFSD AA7050 specimens retain a large fraction of the wrought strength (UTS 428 ± 35 MPa, i.e. ~80–92% of the wrought value ~507 MPa) but exhibit virtually zero uniform elongation and fail abruptly without any observable macroscopic necking. This strong-but-brittle response differs from many friction-stir-based deposition studies on AA7050 and AA7075, where the as-deposited samples typically show reduced strength relative to wrought but still undergo significant elongation before fracture, exhibiting the conventional strain-hardening behavior [17,21,30].

Fractography shows that fracture in the as- deposited AFSD condition is governed by manufacturing defects rather than by the matrix. Low-magnification images (Fig. 8(c) capture the entire fracture cross-section and reveal numerous large, irregular pores and unbonded regions, frequently aligned with interlayer interfaces and oriented perpendicular to the build direction. Some defects reach tens of micrometers in diameter, leaving planar facets and thin ligaments between adjacent pores. These extreme-sized defects act as potent stress concentrators, drastically reducing the strain required for crack initiation [48]. Although all tensile test samples were machined from the same AFSD-deposited AA7050, the variation in pore size and pore fraction within the samples governs their tensile response and the UTS of each as-deposited sample. Despite the macroscopically brittle response, high-magnification images from regions between pores (Fig. 8(d)) show equiaxed dimples, indicating that the AA7050 matrix itself retains its characteristic ductile micro-void nucleation and coalescence behavior. The global fracture response is therefore controlled by the large pores and unbonded regions. This coexistence of locally ductile dimples and defect-controlled facets is consistent with prior observations in high-strength aluminum alloys containing casting or processing defects [47,49–51]. Studies on 7xxx alloys with interdendritic shrinkage cavities or recycling-induced porosity report that large voids initiate cracks at very small strains, leading to low impact toughness and reduced elongation even though much of the fracture surface remains dimpled [51,52]. Lalpoor et al. [51] and Jian et al. [50] showed that such shrinkage cavities in 7xxx alloys act as potent crack initiators and drastically reduce tensile ductility. Similarly, elucidating the effect of porosity on the fracture behavior, Kumar et al. [48] demonstrated in powder-metallurgy Ti–6Al–4V that tensile ductility is governed by the largest defect in the gauge section rather than by average porosity; once a critical pore size is exceeded,

elongation drops sharply, whereas yield and UTS change only modestly. The as-deposited AFSD AA7050 follows the same qualitative trend; the presence of large pores promotes premature crack initiation at very low global strains, thereby limiting the overall ductility of the as-deposited AA7050 [17,53]. AFSD studies on AA7050 and AA7075 generally report fine, dynamically recrystallized microstructures with low porosity, in which mechanical properties can be tuned by post-deposition aging [17,21,30]. In those cases, fracture surfaces show dimples nucleated at intermetallics and precipitates, and ductility remains moderate. By contrast, the as-deposited AFSD AA7050 examined here possesses a ductile matrix that is effectively embrittled by process-induced pores and incomplete interlayer bonding.

HIP fundamentally changes the fracture regime by acting simultaneously on the defect population, precipitate state, and grain structure. After HIP, the UTS decreases to 320 ± 6 MPa from 428 ± 35 in the as-deposited condition. The stress–strain curve of the HIPed sample in Fig. 7 shows a pronounced work-hardening regime and total elongation of 18.4 ± 0.57%, nearly matching the ductility of the wrought sample. A low-magnification image of HIPed specimens (Fig. 8(e)) shows the entire fracture surface and reveals no large pores, unbonded regions, or gross defects, characteristic of the as- deposited AFSD condition. The overall fracture morphology of the HIPed sample is rough and tortuous. High-magnification fractography (Fig. 8(f)) shows a dense population of fine, equiaxed dimples, with individual dimples noticeably smaller than those in the wrought sample and in the dimpled regions of the as-deposited AFSD fracture surfaces. This refinement suggests that, once large lack-of-bond pores have been eliminated by HIP, plastic deformation at fracture is accommodated by the nucleation and growth of a high density of small micro-voids rather than by fewer, larger cavities. HIP homogenizes the microstructure and reduces strain localization through coarsening/dissolution of η/η′ precipitates and relaxation of internal residual stresses [26,54,55]. This enables redistribution of damage over a larger number of finer nucleation sites and thereby promotes a finer dimple scale [26,54–56]. In contrast, the wrought and as-deposited AFSD samples retain larger heterogeneities (coarser constituents in the wrought sample and extreme-sized pores in the AFSD sample) that favor growth of larger dimples or defect-controlled cavities. It can be noted that the extended planar facets associated with large pores in as-deposited AFSD samples are largely eliminated after HIPing. The resulting fracture surface clearly indicates that, after HIP, failure proceeds primarily by homogeneous micro-void nucleation, growth, and coalescence i.e., a matrix-controlled ductile mechanism analogous to that of heat treated or homogenized but highly ductile AA7xxx alloy [50,50,54,55].

The conversion from a pore-dominated to a micro-void coalescence-dominated fracture surface is analogous to the effect of HIP in powder-metallurgy Ti–6Al–4V and solid-state recycled aluminum alloys. In HIPing, the densification eliminates extreme-sized pores and restores ductility to levels comparable with wrought AA7050 [26,48,49,52,57]. In those systems, removal of large defects shifts fracture control from defects to the intrinsic response of the matrix. The present HIPed AFSD AA7050 shows the same behavior, where the large pores/unbonded regions formed during AFSD are healed after HIPing. After HIP, the AFSD AA7050 matrix demonstrates its inherent capacity for ductile micro-void coalescence, leading to elongations similar to wrought AA7050. HIP thus produces a pore-free, more homogeneous microstructure, resulting in lower strength but ductility comparable to the wrought sample and completing the transition from defect-controlled fracture in the as- deposited AFSD condition to matrix-controlled ductile fracture in the HIPed state [58,59].

The reduction in strength of AFSD AA 7050 following HIP, despite the consolidation of voids, is primarily caused by the reduction of strengthening Cu solutes [35,39]. The irreversible formation of coarse $Al_7Cu_2Fe$ precipitates permanently depletes the Cu in the matrix necessary to form fine, homogeneous η' ($MgZn_2$) hardening precipitates during final aging [10,29,35]. In Al–Zn–Mg–Cu alloys, peak strength is primarily associated with a dense distribution of fine GP zones and coherent or semi-coherent η′ precipitates

[11,23,29,30,39]. During HIPing, prolonged high-temperature exposure cause them to dissolve, transform, or coarsen into larger, more widely spaced, and less coherent equilibrium η precipitates, as observed in XRD in Fig. 6 [31,34]. This precipitate morphology significantly reduces the alloy's strengthening capacity[35,40]. Earlier studies have shown that increasing the proportion and refinement of η′ improve strength, whereas transformation toward coarse equilibrium η during over-aging reduces the strengthening efficiency[25,34,35,40].

### 4.2 Effect of Interlayer Porosity on the Effective Tensile Strength in AFSD AA7050

The fractography and pore statistics presented indicate that the loss of ductility in the as-deposited AFSD AA7050 is governed by extreme-sized pores and lack-of-bond defects at interlayer boundaries, rather than by an intrinsically brittle matrix. To quantify this effect, a simple effective-area framework was adopted, schematically illustrated in Fig. 9 (a). In a tensile specimen containing pores within the gauge section, the nominal cross-sectional area $A_n$ is reduced to an effective load-bearing area $A_{eff} = A_n - (Ap1 + Ap2 + \dots)$, where $A_{pi}$ denotes the projected area of each pore intersecting the cross-section. Under an applied tensile load F, the nominal stress recorded during testing is $\sigma_{nom} = F/A_n$, whereas the true stress carried by the intact metal ligaments is $\sigma_{eff} = F/A_{eff}$. When the pore fraction $(f) = \Sigma Api/A_n$ is large, $\sigma_{eff}$ can substantially exceed $\sigma_{nom}$ even if the macroscopic stress–strain curve shows only modest strength reduction.

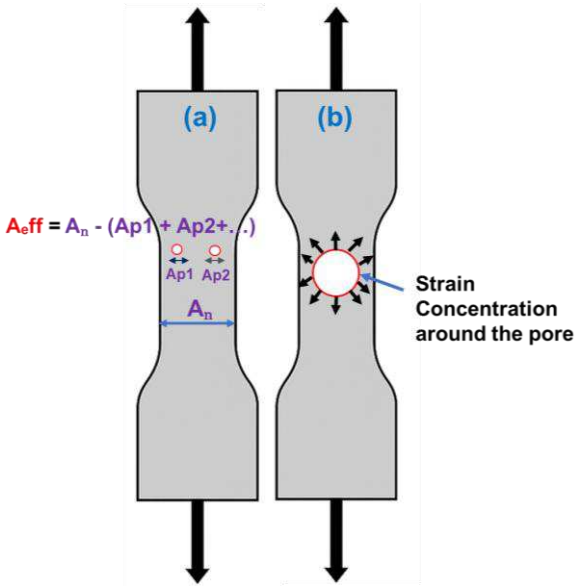



**Fig. 9.** Schematic illustration of (a) a tensile specimen containing interlayer pores within the gauge section, and (b) strain concentration around pore.

The local pore area fractions (*f*) in each fractured AFSD as-deposited tensile specimen were quantified by segmenting all visible voids on the full fracture cross-section using ImageJ Software, measuring the cumulative projected pore area and normalizing it by the total analyzed fracture surface area. The measured pore fractions in the three AFSD as-deposited specimens were therefore used to estimate $A_{eff}$ in the gauge section and to recalculate the UTS referenced to the effective area as given in Table 4. Although the nominal UTS values for AFSD 1–3 are reduced to 468, 410, and 404 MPa, respectively (80–92% of the wrought value of ~506 MPa), the corresponding effective UTS values cluster tightly around ~506 MPa, i.e., essentially identical to the wrought reference. This simple area-correction analysis supports the conclusion that the AA7050 matrix in the AFSD deposits retains its intrinsic tensile strength, and the apparent loss of load-bearing capacity originates from the reduction in effective cross-section and the early onset of void-controlled failure, rather than from microstructural degradation during fabrication.

Table 4. Measured pore area fraction in the gauge section of as-deposited AFSD AA7050 tensile specimens and corresponding nominal and effective ultimate tensile strengths. Effective UTS is calculated by normalizing the maximum load by the reduced effective load-bearing area.

| Sample | Pore Fraction (%) | Nominal UTS (MPa) | Effective UTS (MPa) |
|---|---|---|---|

| | | | |
|---|---|---|---|
| Wrought AA7050 | n.a. | 506.00 | n.a. |
| AFSD 1 AA7050 | 9 | 468.19 | 508.90 |
| AFSD 2 AA7050 | 17 | 410.00 | 506.23 |
| AFSD 3 AA7050 | 20 | 404.24 | 505.30 |

The fracture behavior of as-deposited AFSD AA7050 is explained based on the microstructural features shown in Fig. 9(b). The schematic in Fig. 9(b) shows the local strain concentration that develops around a large pore under uniaxial loading. Under the applied tensile load, the strain concentrates around the pores, creating localized tensile strain concentration zones that exceed the material's local fracture strain[48]. As a result, a crack initiates near the pore, where high strain initiates microcrack formation. They propagate along the interlayer boundaries and coalesce through adjacent void networks, resulting in brittle interlayer fracture. Earlier studies [44,45,48,57] show that the tensile stress in the ligament surrounding a void can be several times higher than the nominal applied stress, and that plastic strain localizes rapidly around the void perimeter once the yielding initiates in the sample. In the critical local strain (CLS) approach proposed for Al–Si cast alloys, clustered interdendritic porosity is replaced by a single equivalent void of area $Av = f * A_{\mathrm{n}}$, where $f$ is the projected pore area fraction; failure is predicted to occur when the local strain at the void reaches a critical value that is essentially independent of $f$ [60]. Within this framework, increasing $f$ reduces the ligament area around the void, raising the local stress/strain for a given $\sigma_{nom}$ and thereby lowering the macroscopic ductility even if the matrix strength remains unchanged. The fact that the effective UTS in Table 4 remains close to that of wrought AA7050 is in good agreement with such CLS models, which attribute the primary role of porosity to geometric amplification of local stress and strain rather than to changes in matrix hardening behavior.

The controlled-defect studies show that tensile strength is relatively insensitive to porosity until a critical local pore area is exceeded, whereas ductility collapses much earlier across a wide range of metals [48,57]. Wilson-Heid et al. [43] introduced single pores into L-PBF 316L and found that UTS was unchanged until the pore occupied ~16% of the cross-section, while elongation fell steeply once the pore area reached ~9%, marking a transition to flaw-controlled fracture with an essentially intact matrix strength. Similar behavior has been reported for L-PBF AlSi10Mg, where fracture strain correlates more strongly with pore fraction measured on the fracture surface than with bulk porosity, and modest changes in local porosity within the necking region produced large drops in elongation [45,60]. Cast and wrought Al 2xxx/7xxx alloys containing shrinkage porosity exhibit the same trend: a few percent projected pore area is sufficient to substantially reduce/halve the fracture strain, while UTS is affected much less and fracture surfaces show a mixture of dimples and large cavities [60]. Together with analogous observations in other alloy systems, these results provide a clear context for the present AFSD AA7050 data where pore fractions of 9–20% in the gauge section almost eliminate uniform elongation, yet the effective UTS corrected for the reduced load-bearing area recovers the wrought strength, indicating that the matrix remains strong and that failure is governed by the size and clustering of large interlayer pores [43,61].

## 5 Conclusions

This study elucidates the coupled effects of friction stir additive manufacturing and hot isostatic pressing (HIP) on the microstructure, defects, and mechanical response of AA7050, benchmarked against a wrought AA7050. By systematically correlating tensile behavior with microstructure, a clear linkage has been established among precipitation, defects, and fracture mechanisms, enabling a critical assessment of AFSD's capabilities and limitations for high-strength AA7050 aluminum alloys.

(i) This study successfully demonstrates the manufacturing of high-density (>99%) AA7050 alloy using the AFSD AM technique. The layers contain coarse recrystallized grains, while interlayers contain ultra-fine equiaxed grains, forming a pronounced layered/bimodal architecture.

(ii) In the as- deposited AFSD condition, the AA7050 recovered a large fraction of the wrought strength, with UTS ≈ 404–468 MPa (≈80–92% of wrought AA7050) but showed zero uniform elongation and no macroscopic necking. The loss of ductility in AFSD AA7050 in the as-deposited condition is attributed to large pores and lack-of-bond regions concentrated near interlayer boundaries, which act as dominant crack initiators.

(iii) The post-processing HIP successfully closed the large interfacial pores in the as- deposited AFSD AA7050 alloy. Also, HIP fundamentally changed the balance between strength and ductility. After HIP, the strength decreased (≈60–65% of the wrought value) while the ductility increased to a level comparable to that of the wrought AA7050. This indicates a transition from defect-controlled to matrix-controlled fracture in HIPed AFSD AA7050 alloy. This mechanical shift is directly driven by microstructural evolution during the HIP thermal cycle: the prolonged high-temperature exposure and subsequent slow furnace cooling caused the primary strengthening phases to coarsen into ~1 μm intragranular hexagonal $MgZn_2$ rods, while inducing morphological rounding of the insoluble, coarse (Fe, Cu)- rich precipitate particles present within the grains and along the grain boundaries.

(iv) This study demonstrates that AFSD can generate a high-strength AA7050 microstructure, but as-deposited performance is critically sensitive to large pores and lack-of-bond defects. HIP effectively removes these defects and restores wrought-like ductility, but at the cost of a substantial reduction in strength. Therefore, optimal AFSD AA7050 processing must control both defect formation and precipitation, using process parameters and toolpaths that reduce the formation of large pores and interlayer lack-of-bond regions. In addition, the thermal processing parameters, including any HIP and aging steps, should be chosen so that the remaining porosity is closed while the strengthening η′/η precipitates are largely preserved.

## CRediT authorship contribution statement

**Krishna P. Joshi:** Methodology, Investigation, Writing, original draft. **Surya T. Bijjala:** Methodology, Investigation, Writing, review & editing. **Anil Lama:** Methodology, Investigation, Formal analysis, Writing, review & editing. **Chad Beamer:** Methodology, Resources, Investigation, review & editing. **Jackson Hise:** Methodology, Resources, Investigation, review & editing. **Nick Palya:** Methodology, Resources, Investigation. **Rumman Ahsan:** Methodology, Resources, Investigation. **Sean Langan:** Methodology, Resources. **Arvind Agarwal:** Conceptualization, Writing, review & editing, Supervision, Funding acquisition. **Tyler Dolmetsch:** Methodology, Investigation, Funding acquisition. **Tanaji Paul:** Methodology, Investigation, review & editing, Supervision. **Sohail M.A.K. Mohammed:** Conceptualization, Methodology, Investigation, Writing, review & editing. **Pankaj Kumar:** Conceptualization, Methodology, Supervision, Writing, review & editing, Funding acquisition.

## Declaration of competing interest

All the authors declare that they have no known conflict of interest.

## Data availability

All the raw data will be made available to the journal on the request.


## Acknowledgements

Krishna Joshi and Pankaj Kumar greatly appreciate the partial financial support from NASA through the New Mexico Space Grant Consortium Research Initiation Grant (Grant Number 80NSSC20M0034). Anil Lama, Sohail M.A.K. Mohammed, Tyler Dolmetsch, Tanaji Paul, gratefully acknowledge support from the DEVCOM – Army Research Laboratory through the W911NF2020256 grant. The usage of facilities at the Advanced Materials Engineering Research Institute (AMERI) is recognized for the research reported in this study.


## References


[1] D.Z. Avery, C.E. Cleek, B.J. Phillips, M.Y. Rekha, R.P. Kinser, H.M. Rao, L.N. Brewer, P.G. Allison, J.B. Jordon, Evaluation of Microstructure and Mechanical Properties of Al-Zn-Mg-Cu Alloy Repaired via Additive Friction Stir Deposition, J. Eng. Mater. Technol 144 (2022). https://doi.org/10.1115/1.4052816.

[2] K.V. Jata, K.K. Sankaran, J.J. Ruschau, Friction-stir welding effects on microstructure and fatigue of aluminum alloy 7050-T7451, Metall Mater Trans A 31 (2000) 2181–2192. https://doi.org/10.1007/s11661-000-0136-9.

[3] J.B. Geisler, R. M. Y., J.E. Strain, L.N. Brewer, J.B. Jordon, P.G. Allison, G.W. Kubacki, Examination of the Corrosion Susceptibility of a Multilayer AA7050 Additive Friction Stir Deposition Build, Journal of Materials Engineering and Performance (2025). https://doi.org/10.1007/s11665-025-11345-9.

[4] N. Habib, A. Vafadar, F. Guzzomi, A comparative study of aluminium properties manufactured using additive friction stir deposition (AFSD) and wire arc additive manufacturing (WAAM), Prog Addit Manuf 10 (2025) 8963–8983. https://doi.org/10.1007/s40964-025-01217-y.

[5] I. Liu, T.C. Bor, P.G. Allison, J.B. Jordon, Additive friction stir deposition of aluminum alloys: A critical review, Materials & Design 258 (2025) 114543. https://doi.org/10.1016/j.matdes.2025.114543.

[6] K.V. Wong, A. Hernandez, A review of additive manufacturing, International Scholarly Research Notices 2012 (2012).

[7] N. Li, S. Huang, G. Zhang, R. Qin, W. Liu, H. Xiong, G. Shi, J. Blackburn, Progress in additive manufacturing on new materials: A review, Journal of Materials Science & Technology 35 (2019) 242–269.

[8] X. Dong, M. Zhou, Y. Geng, Y. Han, Z. Lei, G. Chen, Q. Shi, Recent Advances in Additive Friction Stir Deposition: A Critical Review, Materials 17 (2024) 5205. https://doi.org/10.3390/ma17215205.

[9] P. Deka, Additive Manufacturing: A Brief Study on Selecting Laser Melting Technology, Asian Journal For Convergence In Technology (AJCT) ISSN-2350-1146 8 (2022) 61–68.

[10] Z. Wang, M. Wang, Y. Li, H. Xiao, H. Chen, J. Geng, X. Li, D. Chen, H. Wang, Effect of pretreatment on microstructural stability and mechanical property in a spray formed Al-Zn-Mg-Cu alloy, Materials & Design 203 (2021) 109618. https://doi.org/10.1016/j.matdes.2021.109618.

[11] E.M. Mazzer, C.R.M. Afonso, M. Galano, C.S. Kiminami, C. Bolfarini, Microstructure evolution and mechanical properties of Al–Zn–Mg–Cu alloy reprocessed by spray-forming and heat treated at peak aged condition, Journal of Alloys and Compounds 579 (2013) 169–173. https://doi.org/10.1016/j.jallcom.2013.06.055.

[12] D. Xiao, Z. He, L. Huang, Microstructure and Properties of 7050-T74 Aluminum Alloys with Different Zn/Mg Ratios, Metals 14 (2024) 1226. https://doi.org/10.3390/met14111226.
[13] J. Strain, J.B. Jordon, P. Allison, L.N. Brewer, Evolution of Precipitate Structure and Composition as a Function of Heat Input for Additive Friction Stir Deposition of Aa7050, (2025). https://doi.org/10.2139/ssrn.5119286.
[14] R.S. Mishra, R.S. Haridas, P. Agrawal, Friction stir-based additive manufacturing, Science and Technology of Welding and Joining 27 (2022) 141–165. https://doi.org/10.1080/13621718.2022.2027663.
[15] M.S. El-Sayed, M. Ibrahim, A.I. Abdel-Aziz, Effect of friction stir processing parameters on mechanical properties of different aluminum alloy plates, Sci Rep 15 (2025) 27066. https://doi.org/10.1038/s41598-025-11948-1.
[16] V.A. Rojas, I.Y. Hidalgo, K. Matalgah, T.J. Fleck, L.N. Brewer, G.W. Kubacki, J.B. Jordon, P.G. Allison, Elucidating the Effects of Material Flow from Deposition Offset on AFSD Repair of AA7050, Metals 15 (2025) 164. https://doi.org/10.3390/met15020164.
[17] C.J.T. Mason, R.I. Rodriguez, D.Z. Avery, B.J. Phillips, B.P. Bernarding, M.B. Williams, S.D. Cobbs, J.B. Jordon, P.G. Allison, Process-structure-property relations for as-deposited solid-state additively manufactured high-strength aluminum alloy, Additive Manufacturing 40 (2021) 101879. https://doi.org/10.1016/j.addma.2021.101879.
[18] J. Shao, A. Samaei, T. Xue, X. Xie, S. Guo, J. Cao, E. MacDonald, Z. Gan, Additive friction stir deposition of metallic materials: Process, structure and properties, Materials & Design 234 (2023) 112356. https://doi.org/10.1016/j.matdes.2023.112356.
[19] C. Wu, H. Chen, J. Wang, W. Guo, X. Liu, T. Yang, Additive Friction Stir Deposition of 2219-T8 Lightweight Alloys: Mechanical Performance and Microstucture Formation Mechanism, (2025). https://doi.org/10.2139/ssrn.5749000.
[20] F. Girault, L. Toualbi, Q. Barres, E. Charkaluk, Investigating multi-scale heterogeneity in multi-layer additive friction stir deposition of high-strength aluminum alloys, Materials Science and Engineering: A 927 (2025) 147979. https://doi.org/10.1016/j.msea.2025.147979.
[21] G.D. Hahn, K.P. Knight, N. Gotawala, H.Z. Yu, Additive friction stir deposition of AA7050 achieving forging-like tensile properties, Materials Science and Engineering: A 896 (2024) 146268. https://doi.org/10.1016/j.msea.2024.146268.
[22] G.E. Petter, J.D. Figert, D.J. Rybicki, T. Burns, Heat Treatment of Friction-Stir-Welded 7050 Aluminum Plates, 2006. https://ntrs.nasa.gov/citations/20100014157 (accessed December 2, 2025).
[23] M. Dixit, R. Mishra, K.K. Sankaran, Structure–property correlations in Al 7050 and Al 7055 high-strength aluminum alloys, Materials Science and Engineering: A 478 (2008) 163–172. https://doi.org/10.1016/j.msea.2007.05.116.
[24] X. Xiao, D. Cheng, H. Li, C. Zhang, F. Zhang, A. Qi, Microstructure analysis of 7050 aluminum alloy joint fabricated by linear friction weld, International Journal of Lightweight Materials and Manufacture 7 (2024) 520–530. https://doi.org/10.1016/j.ijlmm.2024.03.008.
[25] F. Guo, B. Zhu, L. Jin, G. Wang, H. Yan, Z. Li, Y. Zhang, B. Xiong, Microstructure and mechanical properties of 7A56 aluminum alloy after solution treatment, Rare Metals 40 (2017) 168–175. https://doi.org/10.1007/s12598-017-0985-7.
[26] M.N. Gussev, N. Sridharan, Z. Thompson, K.A. Terrani, S.S. Babu, Influence of hot isostatic pressing on the performance of aluminum alloy fabricated by ultrasonic additive manufacturing, Scripta Materialia 145 (2018) 33–36. https://doi.org/10.1016/j.scriptamat.2017.10.004.
[27] L. Alqawasmi, S.T. Bijjala, T. Khraishi, P. Kumar, Mechanical property heterogeneity in Inconel 718 superalloy manufactured by directed energy deposition, J Mater Sci 59 (2024) 5047–5065. https://doi.org/10.1007/s10853-023-09249-x.
[28] J.K. Yoder, R.J. Griffiths, H.Z. Yu, Deformation-based additive manufacturing of 7075 aluminum with wrought-like mechanical properties, Materials & Design 198 (2021) 109288. https://doi.org/10.1016/j.matdes.2020.109288.

[29] P. Jia, Y. Cao, Y. Geng, L. He, N. Xiao, J. Cui, Studies on the microstructures and properties in phase transformation of homogenized 7050 alloy, Materials Science and Engineering: A 612 (2014) 335–342. https://doi.org/10.1016/j.msea.2014.06.027.
[30] B. Feng, M.R. Rajanna, J. Lua, G. Hahn, K. Knight, G. Murray, A. Timmons, N. Phan, Multi-stage precipitation modeling for AA 7050 hole repairs in additive friction stir deposition, J. Appl. Phys. 136 (2024) 165102. https://doi.org/10.1063/5.0221890.
[31] F. Chen, J. He, Y. Li, B. Deng, J. Zhu, H. Yang, M. Li, Effect of different homogenization times on the mechanical properties of 7075 aluminum alloy, Journal of Materials Research and Technology 31 (2024) 2582–2592. https://doi.org/10.1016/j.jmrt.2024.07.010.
[32] M. Mohammadtaheri, A New Metallographic Technique for Revealing Grain Boundaries in Aluminum Alloys, Metallogr. Microstruct. Anal. 1 (2012) 224–226. https://doi.org/10.1007/s13632-012-0033-9.
[33] J. Ge, S. Pillay, H. Ning, Post-Process Treatments for Additive-Manufactured Metallic Structures: A Comprehensive Review, Journal of Materials Engineering and Performance 32 (2023) 7073–7122. https://doi.org/10.1007/s11665-023-08051-9.
[34] Y.-L. Deng, L. Wan, Y. Zhang, X.-M. Zhang, Evolution of microstructures and textures of 7050 Al alloy hot-rolled plate during staged solution heat-treatments, Journal of Alloys and Compounds 498 (2010) 88–94. https://doi.org/10.1016/j.jallcom.2010.03.117.
[35] T.-J. Hsiao, P.-H. Chiu, C.-L. Tai, T.-C. Tsao, C.-Y. Tseng, Y.-X. Lin, H.-R. Chen, T.-F. Chung, C.-Y. Chen, S.-H. Wang, J.-R. Yang, Effect of Cu Additions on the Evolution of Eta-prime Precipitates in Aged AA 7075 Al–Zn–Mg–Cu Alloys, Metals 12 (2022) 2120. https://doi.org/10.3390/met12122120.
[36] A. Nicolas, A.W. Mello, M.D. Sangid, Relationships between microstructure and micromechanical stresses on local pitting during galvanic corrosion in AA7050, Corrosion Science 154 (2019) 208–225. https://doi.org/10.1016/j.corsci.2019.03.016.
[37] A.E.A. Chemin, C.M. Afonso, F.A. Pascoal, C.I. dos S. Maciel, C.O.F.T. Ruchert, W.W. Bose Filho, Characterization of phases, tensile properties, and fracture toughness in aircraft-grade aluminum alloys, Material Design & Processing Communications 1 (2019) e79. https://doi.org/10.1002/mdp2.79.
[38] T.-F. Chung, M. Kawasaki, P. Wang, K. Nishio, M. Shiojiri, W.-C. Li, C.-N. Hsiao, J.-R. Yang, Atomic-resolution energy dispersive X-ray spectroscopy mapping of η precipitates in an Al-Mg-Zn-Cu alloy, Materials Characterization 166 (2020) 110448. https://doi.org/10.1016/j.matchar.2020.110448.
[39] H. Fröck, C. Rowolt, B. Milkereit, M. Reich, W. Kowalski, A. Stark, O. Kessler, In situ high-energy X-ray diffraction of precipitation and dissolution reactions during heating of Al alloys, J Mater Sci 56 (2021) 19697–19708. https://doi.org/10.1007/s10853-021-06548-z.
[40] W. Zhao, L. Wang, Y. Ren, B. He, S. Han, P. Xu, Y. Liang, Effect of precipitates evolution on mechanical properties of Al 7050 alloy during secondary aging, Mater. Res. Express 10 (2023) 076502. https://doi.org/10.1088/2053-1591/ace02b.
[41] S. Henninger, R. Chafle, E. Maawad, B. Klusemann, M. Müller, P. Staron, Impact of friction stir welding-like heat cycles on precipitates in AA7050 analysed by SAXS and numerical modelling, Materialia 39 (2025) 102343. https://doi.org/10.1016/j.mtla.2025.102343.
[42] M.J. Styles, T.J. Bastow, M.A. Gibson, C.R. Hutchinson, Substitution of Cu and/or Al in η phase (MgZn2) and the implications for precipitation in Al–Zn–Mg–(Cu) alloys, Intermetallics 49 (2014) 40–51. https://doi.org/10.1016/j.intermet.2014.01.012.
[43] A.E. Wilson-Heid, T.C. Novak, A.M. Beese, Characterization of the Effects of Internal Pores on Tensile Properties of Additively Manufactured Austenitic Stainless Steel 316L, Experimental Mechanics 59 (2019) 793–804. https://doi.org/10.1007/s11340-018-00465-0.
[44] G. Mugica, D. Tovio, J. Cuyas, A. González, Effect of porosity on the tensile properties of low ductility aluminum alloys, Materials Research 7 (2004) 221–229. https://doi.org/10.1590/S1516-14392004000200002.

[45] C.M. Laursen, S.A. DeJong, S.M. Dickens, A.N. Exil, D.F. Susan, J.D. Carroll, Relationship between ductility and the porosity of additively manufactured AlSi10Mg, Materials Science and Engineering. A, Structural Materials: Properties, Microstructure and Processing 795 (2020). https://doi.org/10.1016/j.msea.2020.139922.
[46] G. Chen, X. Ma, X. Yang, W. Huang, J. Zhang, X. Zhu, M. Liu, Y. Qian, J. Zhang, W. Qiu, H. Dong, Multimodal fusion learning for fractrography auto-recognition and uncovering microstructure - fractography relationship in 7050 aluminum alloy, Materials Today Communications 42 (2025) 111402. https://doi.org/10.1016/j.mtcomm.2024.111402.
[47] A.L.M. de Carvalho, J. de P. Martins, Effect of Interrupted Ageing and Retrogression-Reageing Treatments on Fatigue Crack Growth with a Single Applied Overload in 7050 Aluminum Alloy, Mat. Res. 21 (2018) e20170526. https://doi.org/10.1590/1980-5373-MR-2017-0526.
[48] P. Kumar, K.S. Ravi Chandran, F. Cao, M. Koopman, Z.Z. Fang, The Nature of Tensile Ductility as Controlled by Extreme-Sized Pores in Powder Metallurgy Ti-6Al-4V Alloy, Metall Mater Trans A 47 (2016) 2150–2161. https://doi.org/10.1007/s11661-016-3419-5.
[49] J. Cao, F. Li, P. Li, X. Ma, J. Li, Analysis of ductile–brittle competitive fracture criteria for tension process of 7050 aluminum alloy based on elastic strain energy density, Materials Science and Engineering: A 637 (2015) 201–214. https://doi.org/10.1016/j.msea.2015.04.010.
[50] H.G. Jian, X.E. Xie, F. Jiang, J.L. Li, Fractography Analysis on the Fracture Behavior of High Strength Aluminum Alloy, Advanced Materials Research 399–401 (2012) 46–49. https://doi.org/10.4028/www.scientific.net/AMR.399-401.46.
[51] M. Lalpoor, D.G. Eskin, L. Katgerman, Fracture behavior and mechanical properties of high strength aluminum alloys in the as-cast condition, Materials Science and Engineering: A 497 (2008) 186–194. https://doi.org/10.1016/j.msea.2008.06.047.
[52] P. Abachi, P.S.Z. Naseri, K.P. and T.W. Coyle, P. Abachi, P.S.Z. Naseri, K.P. and T.W. Coyle, Fracture Behavior Evaluation of High-Strength 7050 and 7075 Aluminum Alloys Using V-Notched Specimen, in: Fracture Mechanics - Properties, Patterns and Behaviours, IntechOpen, 2016. https://doi.org/10.5772/64463.
[53] Y. Wu, J. Fang, C. Wu, C. Li, G. Sun, Q. Li, Additively manufactured materials and structures: A state-of-the-art review on their mechanical characteristics and energy absorption, International Journal of Mechanical Sciences 246 (2023) 108102. https://doi.org/10.1016/j.ijmecsci.2023.108102.
[54] L. Chang, W. Sun, Y. Cui, R. Yang, Influences of hot-isostatic-pressing temperature on microstructure, tensile properties and tensile fracture mode of Inconel 718 powder compact, Materials Science and Engineering: A 599 (2014) 186–195. https://doi.org/10.1016/j.msea.2014.01.095.
[55] S. Billard, J.P. Fondère, B. Bacroix, G.F. Dirras, Macroscopic and microscopic aspects of the deformation and fracture mechanisms of ultrafine-grained aluminum processed by hot isostatic pressing, Acta Materialia 54 (2006) 411–421. https://doi.org/10.1016/j.actamat.2005.09.012.
[56] H. Niu, Z. Liu, H. Wang, H. Wu, Q. Liu, G. Fan, Effects of hot isostatic pressing on the micron-scale residual stress of nickel-based single-crystal superalloys, Journal of Materials Science & Technology 221 (2025) 102–116. https://doi.org/10.1016/j.jmst.2024.09.036.
[57] P. Kumar, K.S.R. Chandran, Strength–Ductility Property Maps of Powder Metallurgy (PM) Ti-6Al-4V Alloy: A Critical Review of Processing-Structure-Property Relationships, Metall Mater Trans A 48 (2017) 2301–2319. https://doi.org/10.1007/s11661-017-4009-x.
[58] Y.S. Sato, M. Urata, H. Kokawa, K. Ikeda, Hall–Petch relationship in friction stir welds of equal channel angular-pressed aluminium alloys, Materials Science and Engineering: A 354 (2003) 298–305. https://doi.org/10.1016/S0921-5093(03)00008-X.
[59] N. Hansen, Hall–Petch relation and boundary strengthening, Scripta Materialia 51 (2004) 801–806. https://doi.org/10.1016/j.scriptamat.2004.06.002.
[60] C. Cáceres, B.I. Selling, Casting defects and the tensile properties of an Al-Si-Mg alloy, Materials Science and Engineering: A 220 (1996). https://doi.org/10.1016/S0921-5093(96)10433-0.

[61] Z. Song, K. Xiao, S. Xiao, K. Du, Z. Mao, T. Li, B. Wang, Effect of porosity on the tensile strength and Micromechanisms of laminated stitched C/C-SiC composites, Materials & Design 247 (2024) 113429. https://doi.org/10.1016/j.matdes.2024.113429.

## Supplementary Files

This is a list of supplementary files associated with this preprint. Click to download.

- Highlights.docx